

Shaping Diverted Plasmas With Symplectic Maps

Geraldo Roberson, Marisa Roberto, Iberê Luiz Caldas, Tiago Kroetz, and Ricardo Luiz Viana

Abstract—We construct an area preserving and integrable map to represent magnetic surfaces with triangularity in single-null divertor tokamaks. The magnetic surfaces obtained by the map can assume different asymmetric geometries and the position of X-point, through the choices of values for some free parameters. The safety factor profile is independent of the geometric parameters and can also be chosen arbitrarily. We combine the divertor integrable map with a nonintegrable map that simulates the effect of external magnetostatic perturbations. The application of this methodology permits to obtain the escape patterns of magnetic field lines on the divertor plates.

Index Terms—Divertor, escape, plasma shape.

I. INTRODUCTION

IN tokamak plasmas, the magnetic field lines wind around isobaric toroidal surfaces called magnetic surfaces [1]. The shape of cross section of these magnetic surfaces plays an important role on plasma stability and confinement in fusion reactors [2]. Moreover, divertor tokamaks present an ideal separatrix with one or two X-points, which separate the closed from the open surfaces, define the plasma border, and divert the particles which escape from the plasma to the divertor plates [3]. External and internal resonances between plasma and perturbation magnetic fields replace the ideal separatrix by a stochastic layer of chaotic magnetic field lines, which are guided to the collector plates [4], [5]. The escaping ions recombine at the plates forming a neutral gas, which can be pumped away from the reactor interior. The divertor of ITER is designed to withstand a heat load of $5 - 10 \text{ MW/m}^2$ coming from alpha particles resulting from fusion reactions taking place in the plasma core [6]. The equilibrium description of these surfaces uses large codes based on numerical solutions of Grad-Shafranov equation [7], [8]. This methodology, although necessary for the careful design of the divertor plates, is too time-consuming for studying basic phenomena related to the field line dynamics near the separatrix.

A discrete mapping of magnetic field lines is obtained from the iteration of recurrence equations that provide the

intersections of magnetic field lines with a plane defined by considering a constant toroidal angle. The main advantage of symplectic maps is to represent hamiltonian systems, which require small computer time to obtain a large number of intersection points, and is particularly useful in numerical studies of transport and escape in the tokamak edge region [9], [10].

Accordingly, a sizeable number of previous investigations have used discrete maps to investigate phenomenological aspects of field lines and pattern deposition in divertor configurations. Some of these maps were obtained directly from the magnetic field equations [11]–[14] from a procedure of generalized Poincaré integrals described in [15]. Other divertor maps were obtained from a mathematical construction of appropriate generating functions and canonical transformations [16]–[19]. Unfortunately, the discretization procedure used in these maps inserts a nonphysical perturbation, which is proportional to the discretization parameter. Recently, Punjabi and coworkers have developed divertor maps with the same topology of DIII-D surfaces by fitting experimental data of discharges in order to find appropriate expressions for the equilibrium Hamiltonian [20]–[24].

However, in the above procedures to obtain discrete mappings for diverted tokamaks, there are limitations on the plasma shape, which makes some of the previous mappings too particularly related to given geometries. In order to overcome these limitations, we obtained in this paper integrable and symplectic maps, which can represent equilibrium magnetic surfaces in a single null divertor tokamak, such that the geometry of the separatrix (and consequently the internal and external surfaces) can be tailored by free parameters that give magnetic surfaces with triangularity. The safety factor associated to the surfaces can also be chosen independently of the geometry configuration adopted. The mappings have been obtained from the trajectory integration method originally introduced to describe single-null diverted tokamaks [25], [26].

This paper is organized as follows. In Section II, we outline the basics of the method used for obtaining the field line map. Section III presents an application of the divertor map so obtained with a magnetic perturbation caused by a resonant magnetic perturbation (RMP), as well as in our numerical results. Section IV presents the conclusions.

II. DIVERTOR FIELD LINE MAPPING

A. Trajectory Integration Method

The trajectory integration method of discrete map construction was initially applied to obtain a single-null divertor maps, but with a little freedom of equilibrium configuration choices [25], [26]. The improvement on the methodology presented in this paper is to consider a modification that

Manuscript received October 15, 2016; revised December 13, 2016; accepted December 27, 2016. This work was supported in part by the São Paulo Research Foundation (FAPESP), Brazil, under Grant 2015/16471-8 and Grant 2011/19296-1, in part by CNPq, Brazil, under Grant 446905/2014-3, and in part by CAPES, Brazil.

G. Roberson and M. Roberto are with the Departamento de Física, Instituto Tecnológico de Aeronáutica, São José dos Campos 12228-900, Brazil (e-mail: ger_rca@yahoo.com.br; marisar@ita.br).

I. L. Caldas is with the Instituto de Física, University of São Paulo, São Paulo 05315-970, Brazil (e-mail: ibere@if.usp.br).

T. Kroetz is with the Departamento de Física, Universidade Tecnológica Federal do Paraná, Pato Branco 85503-390, Brazil (e-mail: kroetz@utfpr.edu.br).

R. L. Viana is with the Departamento de Física, Universidade Federal do Paraná, Curitiba 81531-990, Brazil (e-mail: viana@fisica.ufpr.br).

Color versions of one or more of the figures in this paper are available online at <http://ieeexplore.ieee.org>.

Digital Object Identifier 10.1109/TPS.2017.2649882

allows the construction of asymmetric integrable surfaces with a given shape. As a consequence, the map we are to obtain can represent magnetic surfaces of a plasma column with triangularity.

Basically, the procedure to obtain the map can be summarized as follows. The first step is a choice of an adequate expression $V(x, y)$ in a field-line Hamiltonian

$$\Psi(x, y) = \frac{x^2}{2} + V(x, y) \quad (1)$$

with maxima and minima located in appropriate values of x and y . These positions correspond to the elliptic and hyperbolic fixed points in the phase space for the magnetic surface shape we want to describe. The Hamiltonian (1) is integrable and $V(x, y)$ must allow analytical solutions for the Hamilton equations

$$\frac{dy}{dt} = \frac{\partial \Psi}{\partial x} \quad \frac{dx}{dt} = -\frac{\partial \Psi}{\partial y}. \quad (2)$$

From the latter, an auxiliary expression can be used to generate closed surfaces with the topology desired for the magnetic surfaces represented by the map. In order to obtain asymmetric surfaces in the x -direction, the expression $V(x, y)$ must present a dependence on both spatial variables. A simple way to fulfill the requirement of analytical solutions for the Hamilton equations is to suppose a piecewise dependence for $V(x, y)$ on the x -variable. Proceeding this way, we are able to find the continuous solutions $[x(x_i, y_i, t); y(x_i, y_i, t)]$, where x_i and y_i are the initial conditions for solutions, and to discretize these continuous solutions by making the transformation $[x(x_i, y_i, t); y(x_i, y_i, t)] \rightarrow [x_{n+1}(x_n, y_n, \Delta); y_{n+1}(x_n, y_n, \Delta)]$, in such a way that the resulting equations compose the discrete map equations. The parameter Δ is related to the rotation rate of points on the surface of section, given by the safety factor of the corresponding magnetic surface. Since the surface topology and the fixed points are independent of Δ , we can reproduce any desirable safety factor profile by imposing an appropriate dependence $\Delta(\Psi)$ independently of the chosen geometry.

B. Equilibrium Model

1) *Geometry*: We need a double-well shaped $V(x, y)$, with different depths for positive and negative values of x , in order to create curves in phase space that exhibits two closed regions delimited by a separatrix between them, as single null magnetic surfaces. The expression for $V(x, y)$ with the desired properties will be written as two sets of six parabolas smoothly joint in the connection points, so as to ensure the integrability of the Hamilton equations. The first set represents the region of plasma at the inner side of the tokamak chamber, by considering the negative values of x . The second set of parabolas represents the region of plasma at the outer side of the tokamak chamber, and corresponds to positive the x -values. The continuous solutions for Hamilton equations in each region will be oscillatory in t for positive concavity of $V(x, y)$ with respect to y , and hyperbolic for regions of negative concavity relatively to the y -variable. The large number of

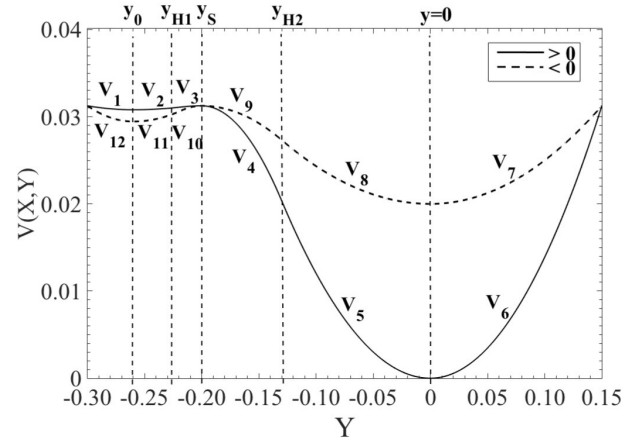


Fig. 1. Function $V(x, y)$ used by the method. Solid dotted line: positive (negative) values of x . Six parabolic branches compose each curve.

pieces so obtained offers a number of free parameters capable to adjust the geometry of the surfaces with a high flexibility.

The expressions for $V(x, y)$ in each one of the regions are given by

$$\begin{aligned} & [a_1(y - y_0)^2]/2 + b_2, \quad y \leq y_0 \quad \text{and} \quad x > 0 \\ & [a'_1(y - y_0)^2]/2 + b'_2, \quad y \leq y_0 \quad \text{and} \quad x < 0 \\ & [a_2(y - y_0)^2]/2 + b_2, \quad y_0 \leq y \leq y_{H1} \quad \text{and} \quad x > 0 \\ & [a'_2(y - y_0)^2]/2 + b'_2, \quad y_0 \leq y \leq y_{H1} \quad \text{and} \quad x < 0 \\ & -[a_3(y - y_S)^2]/2 + b_1, \quad y_{H1} \leq y \leq y_S \quad \text{and} \quad x > 0 \\ & -[a'_3(y - y_S)^2]/2 + b_1, \quad y_{H1} \leq y \leq y_S \quad \text{and} \quad x < 0 \\ & -[a_4(y - y_S)^2]/2 + b_1, \quad y_S \leq y \leq y_{H2} \quad \text{and} \quad x > 0 \\ & -[a'_4(y - y_S)^2]/2 + b_1, \quad y_S \leq y \leq y_{H2} \quad \text{and} \quad x < 0 \\ & a_5 y^2/2, \quad y_{H2} \leq y \leq 0 \quad \text{and} \quad x > 0 \\ & a'_5 y^2/2 + b'_1, \quad y_{H2} \leq y \leq 0 \quad \text{and} \quad x < 0 \\ & a_6 y^2/2, \quad 0 \leq y \quad \text{and} \quad x > 0 \\ & a'_6 y^2/2 + b'_1, \quad 0 \leq y \quad \text{and} \quad x < 0. \end{aligned} \quad (3)$$

We show in Fig. 1 the curve of $V(x, y)$ for a set of geometric parameters values. The figure also shows the connection points y_0 , y_{H1} , y_S , and y_{H2} delimiting the regions of $V(x, y)$.

The continuous trajectories can be obtained by solving (2) in each parabolic region. The internal plasma surfaces will correspond to the solutions for $y > y_S$ and $\Psi < b_1$ while the private flux surfaces will correspond to the solutions for $\Psi < b_1$ and $y < y_S$. The external surfaces present $\Psi > b_1$. After applying the discretization procedure, we obtain the map equations described on the Appendix.

For our objectives, we intend to relate the parameters in the above expressions with geometric parameters that describe the separatrix formed in phase space for the solutions of Hamilton equations. The geometric parameters possible to be fitted are: x_{MAX} , x'_{MAX} , x_{MIN} , x'_{MIN} , y_{MAX} , y_{MIN} , y_0 , y_{H1} , y_{H2} , and y_S . The meaning of each one of these parameters can be observed in Fig. 2.

The relations between the geometric parameters of separatrix and the parameters in (3) defining $V(x, y)$ can be found by keeping in mind the continuity requirement of $V(x, y)$ and its

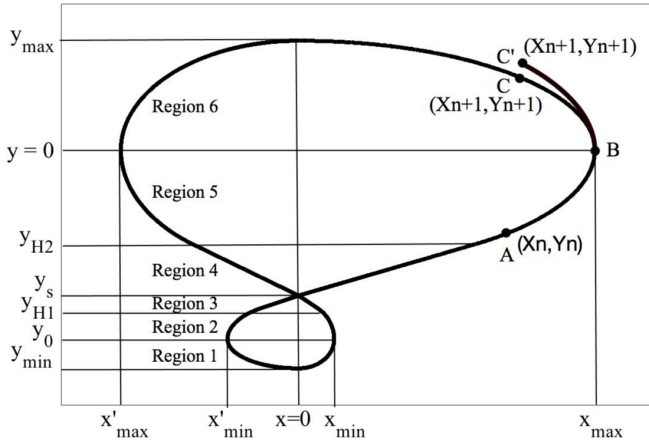


Fig. 2. Schematic of the separatrix revealing the regions, where the function $V(x, y)$ is described by different parabolas and the geometric interpretation of parameters x_{MAX} , x'_{MAX} , x_{MIN} , x'_{MIN} , y_{MAX} , y_{MIN} , y_0 , y_{H1} , y_{H2} , and y_s .

first derivative. The relations obtained through this procedure are

$$\begin{aligned}
 b_1 &= \frac{x_{\text{MAX}}^2}{2}, & b_2 &= b_1 - \frac{x_{\text{MIN}}^2}{2} \\
 b'_1 &= b_1 - \frac{x'^2_{\text{MAX}}}{2}, & b'_2 &= b_1 - \frac{x'^2_{\text{MIN}}}{2} \\
 a_1 &= \frac{x_{\text{MIN}}^2}{(y_{\text{MIN}} - y_0)^2}, & a'_1 &= a_1 + \frac{2(b_2 - b'_2)}{(y_{\text{MIN}} - y_0)^2} \\
 a_2 &= \frac{x_{\text{MIN}}^2}{(y_{H1} - y_0)(y_s - y_0)}, & a'_2 &= -a'_3 \frac{y_{H1} - y_s}{(y_{H1} - y_0)} \\
 a_3 &= \frac{-x_{\text{MIN}}^2}{[(y_{H1} - y_0)(y_{H1} - y_s) - (y_{H1} - y_s)^2]} \\
 a'_3 &= \frac{2(b'_2 - b_1)}{[(y_{H1} - y_s)(y_{H1} - y_0) - (y_{H1} - y_s)^2]} \\
 a_4 &= \frac{x_{\text{MAX}}^2}{(y_{H1} - y_0)^2 - y_{H2}(y_{H2} - y_s)} \\
 a'_4 &= \frac{2(b_1 - b'_1)}{y_s^2 - y_s y_{H2}}, & a_5 &= \frac{x_{\text{MAX}}^2}{y_{H2} y_s} \\
 a'_5 &= -a'_4 \frac{y_{H2} - y_s}{y_{H2}}, & a_6 &= \frac{x_{\text{MAX}}^2}{y_{\text{MAX}}^2}, & a'_6 &= a_6 - \frac{2b'_1}{y_{\text{MAX}}^2}.
 \end{aligned} \tag{4}$$

The map equations are obtained from the discretization of continuous solutions for each considered region, but these equations are not able to map a point from a specific region indicated in (3) to another. As an example, we cannot use the discretized solutions of Hamilton equations to map (x_n, y_n) into (x_{n+1}, y_{n+1}) if $y_n < 0 < y_{n+1}$. This situation is shown in Fig. 2. The map equations we used in this case must change to the correspondent value of $V(x, y)$ in the correct region at the exact point of transition from one region to another. To do this change, we need the value $x_{y=0}$ of the corresponding connection point and the fraction of the discrete parameter Δ necessary to go from (x_n, y_n) to $(x_{y=0}, y=0)$. In the example shown in Fig. 2, the transition occurs from regions 5 to 6. After computing $x_{y=0}$ and the fraction of Δ , we can use the map equations corresponding to region 6. There results a

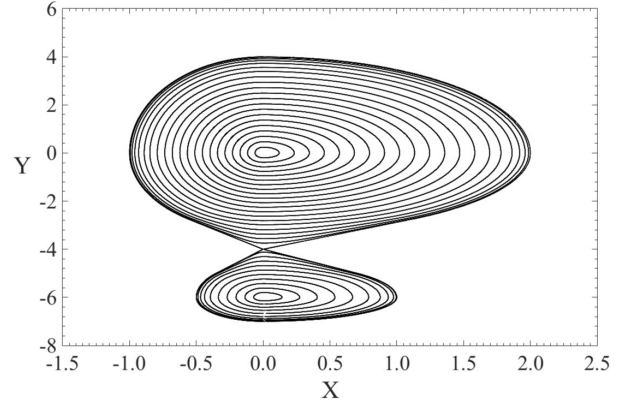


Fig. 3. Poincaré map for geometric parameters $x_{\text{MAX}} = 2$, $x'_{\text{MAX}} = -1.0$, $x_{\text{MIN}} = 1$, $x'_{\text{MIN}} = -0.5$, $y_{\text{MAX}} = 4$; $y_{\text{MIN}} = -7$, $y_{H1} = -5$, $y_{H2} = -2.75$, $y_s = -4$ e, and $y_0 = -6$.

connection map, which is used to accomplish the transition between regions 5 and 6. The complete expression of $V(x, y)$ presents 12 connection points. Therefore, the complete integrable map will be composed of 24 parts.

Some of the invariant surfaces traced with the map are shown in Fig. 3 for geometric parameters described in the caption. All the geometric parameters are in meters. We choose these in order to obtain asymmetric integrable surfaces with a large triangularity. As the topology does not depend on Δ values, we fix $\Delta = 1$ for all surfaces.

2) *Safety Factor Profile*: The continuous solution for the Hamiltonian expressed in (1) presents the same invariant curves in phase space of the magnetic surfaces we want to map. When we substitute the continuous time t by a discrete parameter Δ with a dependence on Ψ , the resulting map presents winding numbers (inverse of safety factor) typically different from the original continuous system and can be arbitrarily set by choosing a dependence $\Delta(\Psi)$ without affecting the chosen topology.

However, the winding number of the original continuous system must be known in order to change to the desirable safety factor profile. If we adopt $\Delta = 1$ for all values of Ψ , the map will present a safety factor profile identical to the period of rotation associated with the continuous system. We must use a Δ value equal to

$$\Delta = \frac{T(\Psi)}{q(\Psi)} \tag{5}$$

to change the original rotation of a surface Ψ , where $T(\Psi)$ is the rotation period of invariant surfaces $\Psi = \text{const.}$ associated with continuous system and $q(\Psi)$ is the safety factor of magnetic surface we intend to represent by the invariant curve $\Psi = \text{const.}$. The function $T(\Psi)$ can be found by obtaining the “time” spent (measured in the number of map iterations) by the continuous trajectory in each region. After determining Δ , we find the analytical expression for the rotation period associated with the surfaces. There will be different expressions for each Ψ interval.

Since the function $T(\Psi)$ is known, we apply any safety factor profile $q(\Psi)$ in (5) and represent different equilibrium configurations with total freedom of choice the plasma shape.

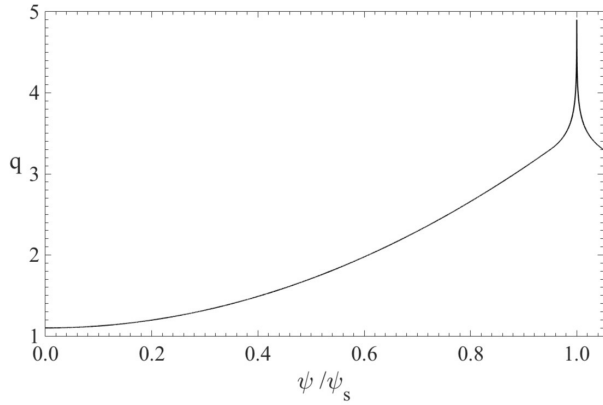


Fig. 4. Safety factor profile model for the plasma region surfaces $\Psi/\Psi_S < 1$ and external surfaces to the separatrix $\Psi/\Psi_S > 1$. We use the parameters $q(0) = 1.1$, $q_{95} = 3.3$, and $\hat{s}_{95} = 2.67$.

If we do not have an analytical expression for the safety factor profile, it turns out that even a table of discrete values of $q(\Psi)$ can be applied to this relation. For simplicity, we choose a monotonic profile for the safety factor with singularity at $\Psi = \Psi_S$. The expression of $q(\Psi)$ with these features can be algebraic until Ψ_{95} and logarithmic between Ψ_{95} and Ψ_S

$$q(\Psi) = \begin{cases} q_0 + c_1\Psi + c_2\Psi^2, & \Psi \leq \Psi_{95} \\ \alpha \ln(\Psi_S - \Psi) + \beta, & \Psi > \Psi_{95}. \end{cases} \quad (6)$$

We opted to choose the following free parameters: $q_0 = q(\Psi = 0)$, q_{95} , and q'_{95} , where we define q'_{95} as the derivative of safety factor profile with respect to Ψ taken at $\Psi = \Psi_{95}$, and q_{95} is the safety factor value at Ψ_{95} .

The magnetic shear of the surface $\Psi_{95} = \text{const.}$ is defined in terms of the local derivative of q as follows:

$$\hat{s}_{95} = \frac{r_{95}}{q_{95}} \left. \frac{dq}{dr} \right|_{r_{95}} \quad (7)$$

where r_{95} is the minor radius of the $\Psi_{95} = \text{const.}$ curve at midplane, which is given by $r_{95} = \sqrt{2\Psi_{95}}$. On applying the chain rule, we relate the shear \hat{s}_{95} with the derivative q'_{95} by

$$q'_{95} = \frac{q_{95}\hat{s}_{95}}{2\Psi_{95}}. \quad (8)$$

The constants on (6) can be related with the free parameters by smoothness condition of $q(\Psi)$ at Ψ_{95}

$$c_1 = \frac{2(q_{95} - q_0) - q'_{95}\Psi_{95}}{\Psi_{95}} \quad (9)$$

$$c_2 = \frac{q_0 - q_{95} + q'_{95}\Psi_{95}}{\Psi_{95}^2} \quad (10)$$

$$\alpha = q'_{95}(\Psi_{95} - \Psi_S) \quad (11)$$

$$\beta = q_{95} - q'_{95}(\Psi_{95} - \Psi_S) \ln(\Psi_S - \Psi_{95}). \quad (12)$$

The model for the external region surface ($\Psi > \Psi_S$) was considered reflected at $\Psi = \Psi_S$. In Fig. 4, we depicted two safety factor profiles, both using $q_0 = 1.1$ and $q_{95} = 3.3$, with shear parameter value at Ψ_{95} . We considered $\hat{s}_{95} = 2.67$.

III. NUMERICAL APPLICATION

We simulate the effect of an RMP in order to show how the divertor map can be used to study the field line dynamics of the stochastic layer. An arrangement of external currents to the plasma creates a perturbing magnetic field that is stronger in the vicinity of tokamak wall and decays exponentially as it penetrates into the tokamak plasma [27]–[29]. One design for the RMP consists of m pairs of conductors carrying electric currents in the opposite toroidal directions [30], [31]. These currents are located at a specific toroidal position and occupy a thin toroidal section.

The impulsive character of the resonant perturbation allows us to compose a map by the integrable divertor map followed by a perturbative map. The integrable divertor map application represents a toroidal turn of a magnetic field line through the tokamak until the RMP position. The next application of a perturbative map represents the mapping of a field line just before the RMP region to after this region. The model proposed by Martin and Taylor [32] consists of a perturbed map written in the coordinates (ρ, α) related to the poloidal coordinates (r, θ) through $\rho = r_c - r$ and $\alpha = r_c\theta$, where r_c is the minor radius of the tokamak chamber. A field line entering the RMP at (ρ_1, α_1) emerges from it at (ρ_2, α_2) , where

$$\alpha_2 = \alpha_1 - C e^{-m\rho_1/r_c} \cos\left(\frac{m\alpha_1}{r_c}\right) \quad (13)$$

$$\rho_2 = \rho_1 + \frac{r_c}{m} \ln \left\{ \cos\left[\frac{m\alpha_1}{r_c}\right] - C \frac{m}{r_c} e^{-m\rho_1/r_c} \cos\left(\frac{m\alpha_1}{r_c}\right) \right\} - \frac{r_c}{m} \ln \left[\cos\left(\frac{m\alpha_1}{r_c}\right) \right]. \quad (14)$$

The constant C in (14) stands for the perturbation amplitude and is related to the physical parameters by $C = \mu_0 g m I_h / \pi r_c B_0$, where μ_0 is the permeability of free space, I_h is the current flowing on the limiter segments, and B_0 is the equilibrium toroidal field. In our simulations, we fix $C = 10^{-2}$, $r_c = 5$, and $m = 3$ and use parameters from the safety factor profiles equilibrium shown in Fig. 4. By applying the maps, we calculate $(x_n, y_n) \rightarrow (x^*, y^*)$ through the integrable divertor map M_D followed by the application of the perturbing map M_P , which gives $(x^*, y^*) \rightarrow (x_{n+1}, y_{n+1})$. It requires a change of Δ value each time the field line emerges from the limiter region, since after the impulsive perturbation, the field lines jump to another magnetic surface $\Psi(x_{n+1}, y_{n+1})$, which has a different safety factor. So, we must apply (5) to select a correct Δ parameter so as to map the field line to the next toroidal turn.

A. Plasma Surface of Section

The phase portrait shown in Fig. 5 was obtained by considering 55 initial conditions along the line $x = 0$ in the interval $y = [-4, -2]$, each one considered during 10^6 iterations. As we expected, although all the initial conditions are taken in the plasma region, some chaotic magnetic field lines close to border occupy a region external to the ideal separatrix. The ideal separatrix was replaced by a stochastic layer, which fills a phase space area depending on the intensity of perturbation.

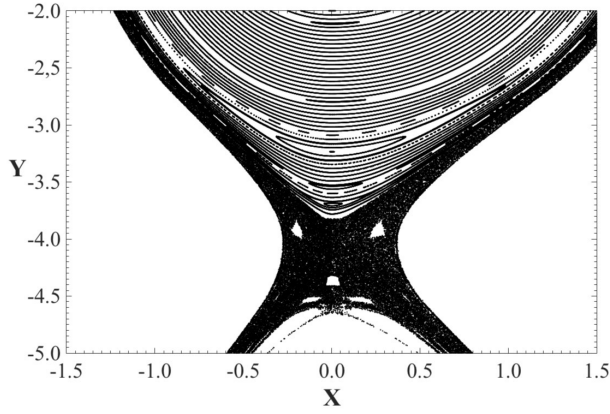


Fig. 5. Poincaré map for perturbation parameters $C = 10^{-2}$ and $m = 3$ for the equilibrium $\delta_{95} = 2.67$. The geometric parameters are the same of Fig. 3.

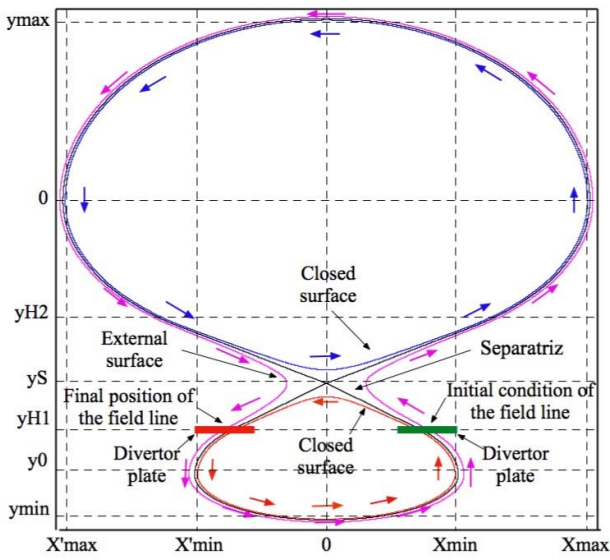


Fig. 6. Schematic of the dynamics exhibited by the map in different regions. To obtain the escape pattern, we consider initial conditions at x_{MIN} and y_{H1} and the escape is defined at the position x_{MIN} and y_{H1} .

The position $y = -5$ is where we imagine to be located a collector plate reached by the escaping magnetic field lines.

B. Perturbed Escape Pattern

Since the divertor plates intercept the chaotic region, which replaced the separatrix in the presence of the RMP, it is important to understand the perturbed escape pattern toward the divertor plates. In particular, since we want to avoid highly localized thermal loads, it is necessary to see if the deposition pattern at the divertor plates is more or less uniform. These deposition patterns are called magnetic footprints and are usually characterized by very irregular stripped patterns [33]–[37]. Moreover, field lines that take a long time (measured in the number of map iteration) to hit the divertor plates may come from the core of the chaotic region, thus bringing energetic particles to the divertor plates.

In Fig. 6, we show schematically the type of escape we are dealing with. There are two divertor plates, a green one and a red one at y_{H1} , symmetrically located with respect to the

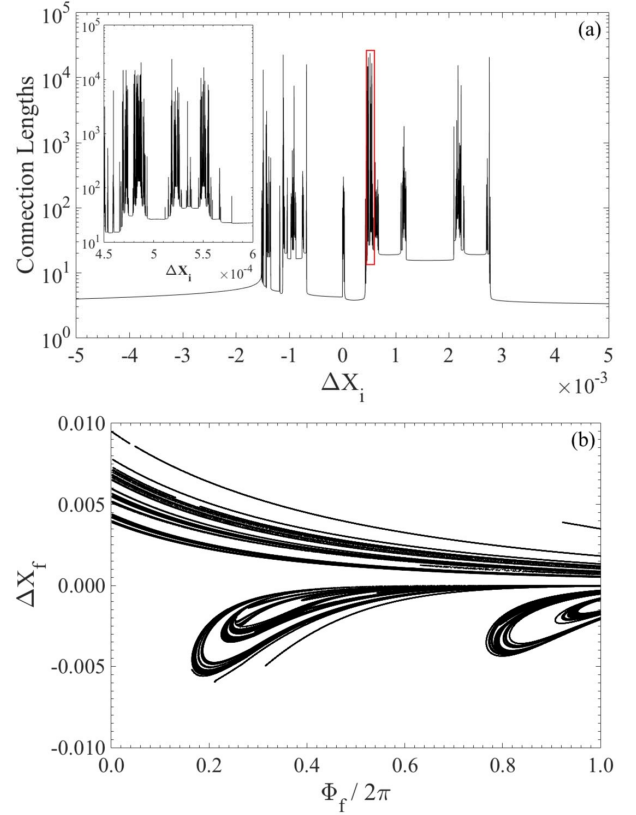


Fig. 7. Escape pattern of magnetic field lines on the collector plate for the case shown in Fig. 5 in terms of (a) connection lengths distribution at the collector plate, where the rectangle indicates an enlargement shown at the corner of the figure, and (b) footprint of magnetic field lines.

x -point, at the points x_{min} and x'_{min} . An initial condition placed on the green plate is expected to evolve through a chaotic orbit originated in the vicinity of the separatrix and it eventually reaches the red plate.

The number of toroidal turns necessary for the field line to reach the divertor plates is called the connection length, which is given by

$$C_L = N + \frac{t_F}{\Delta_N} \quad (15)$$

where N is an integer number of toroidal turns before we stop the iteration to locate the exact hitting point and $\Delta_N = \Delta(\Psi(x_n, y_n))$, which corresponds to Δ parameter for the considered surface, since the trajectories can have perturbations along its trajectory. Note that the magnetic field lines start trajectories in coordinates (x_i, y_{H1}, Φ_i) near nonperturbed separatrix (green plate in Fig.6) and end trajectories at coordinates (x_F, y_{H1}, Φ_F) (red plate in Fig.6). The position x_F , the exact final position of the field line can be calculated using the continuous version of map equations to then calculate the “time” t_F . Thus, the field line takes this “time” until it reaches the plate at the final toroidal angle Φ_F , which is given by

$$\Phi_F = 2\pi \frac{t_F}{\Delta_n}. \quad (16)$$

The distribution of connection lengths on the collector (red) plate as a function of the initial position (on the green divertor plate) is shown in Fig. 7(a). This distribution is

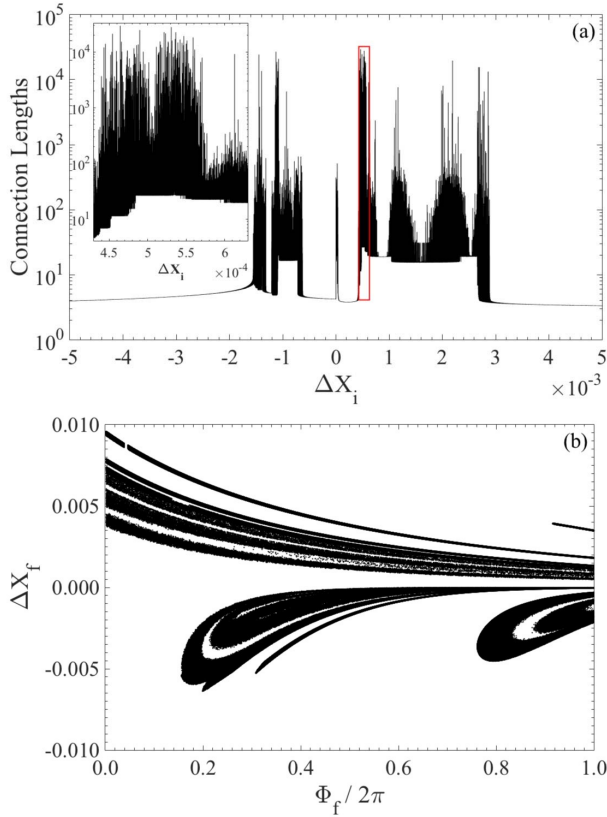


Fig. 8. Same of Fig. 7 considering the collision effect. The collisional amplitude is 1×10^{-4} .

highly nonuniform, presenting a large number of sharp peaks with an apparently fractal distribution (the effect can be best appreciated by the magnification shown in the inset). Moreover, although most of the escaping field lines have small connection lengths (between 3 and 100 toroidal turns), in the sharp peaks, we can have field lines with connection lengths higher than 10^4 . This is particularly important, since the latter are expected to carry energetic particles from the plasma core and the corresponding heat loadings are higher on the divertor plates. The combination of large heat loading with irregular distribution leads to localized attacks that may damage the divertor plates during the operation of the tokamak. The magnetic footprints related to this situation are shown in Fig. 7(b), where we can see the apparent fractal distribution of the loadings.

In the above description, we consider that the plasma particles follow the magnetic field lines, which is a lowest-order approximation, since the various drifts are neglected. If the collision time is larger than the mean characteristic time, it is also possible to neglect the effect of particle collisions. However, if the plasma is dense enough, we have to take into account the collisional effect, which can be done by adding a noisy term in the divertor field line mapping [38], [39].

The effect of collisions in the connection length distribution and in the magnetic footprints is shown in Fig. 8(a) and (b), respectively. We choose a collisional amplitude a value of 1×10^{-4} , which is roughly related to nonuniform temperature profile in ITER [40], [41]. We observe that the chief effect

of the collisions is that the particles suffer a dispersion proportional to the noise level and thus the magnetic footprints become blurry thanks to it. Moreover, the distribution of the connection lengths, although continue to be highly uniform, does not exhibit the fractality (or self-similarity) present in the noiseless case.

IV. CONCLUSION

We present in this paper, an integrable map capable to reproduce magnetic field lines dynamics in asymmetric single-null divertor tokamaks. The advantages of the map are: ensure the symplectic and nonperturbed character of equilibrium configuration with triangularity and safety factor profile with great freedom, independence of geometry and safety factor profile, and the possibility of composition with other perturbed map, which can simulate the effects of different resonances. The field line strike position between consecutive iterations can be naturally obtained by using the continuous version of map equations. This map can be used to investigate the dependence of stability and deposition patterns in terms of different equilibrium parameters.

APPENDIX

DIVERTOR MAP EQUATIONS

The equation of asymmetric divertor map for each region is as follows.

- 1) For $y_n < y_0$

$$\begin{aligned} x_{n+1} &= -(y_n - y_0)\sqrt{a} \sin(\sqrt{a}\Delta) + x_n \cos(\sqrt{a}\Delta) \\ y_{n+1} &= (y_n - y_0) \cos(\sqrt{a}\Delta) + \frac{x_n}{\sqrt{a}} \sin(\sqrt{a}\Delta) + y_0 \end{aligned}$$

where $a = a_1$ for $x > 0$ and $a = a'_1$ for $x < 0$.

- 2) For $y_0 < y_n < y_{H1}$

$$\begin{aligned} x_{n+1} &= -(y_n - y_0)\sqrt{a} \sin(\sqrt{a}\Delta) + x_n \cos(\sqrt{a}\Delta) \\ y_{n+1} &= (y_n - y_0) \cos(\sqrt{a}\Delta) + \frac{x_n}{\sqrt{a}} \sin(\sqrt{a}\Delta) + y_0 \end{aligned}$$

where $a = a_2$ for $x > 0$ and $a = a'_2$ for $x < 0$.

- 3) For $y_{H1} < y_n < y_S$

$$\begin{aligned} x_{n+1} &= (y_n - y_S)\sqrt{a} \sinh(\sqrt{a}\Delta) + x_n \cosh(\sqrt{a}\Delta) \\ y_{n+1} &= (y_n - y_S) \cosh(\sqrt{a}\Delta) + \frac{x_n}{\sqrt{a}} \sinh(\sqrt{a}\Delta) + y_S \end{aligned}$$

where $a = a_3$ for $x > 0$ and $a = a'_3$ for $x < 0$.

- 4) For $y_S < y_n < y_{H2}$

$$\begin{aligned} x_{n+1} &= (y_n - y_S)\sqrt{a} \sinh(\sqrt{a}\Delta) + x_n \cosh(\sqrt{a}\Delta) \\ y_{n+1} &= (y_n - y_S) \cosh(\sqrt{a}\Delta) + \frac{x_n}{\sqrt{a}} \sinh(\sqrt{a}\Delta) + y_S \end{aligned}$$

where $a = a_4$ for $x > 0$ and $a = a'_4$ for $x < 0$.

- 5) For $y_{H2} < y_n < 0$

$$\begin{aligned} x_{n+1} &= -y_n\sqrt{a} \sin(\sqrt{a}\Delta) + x_n \cos(\sqrt{a}\Delta) \\ y_{n+1} &= y_n \cos(\sqrt{a}\Delta) + \frac{x_n}{\sqrt{a}} \sin(\sqrt{a}\Delta) \end{aligned}$$

where $a = a_5$ for $x > 0$ and $a = a'_5$ for $x < 0$.

6) For $y_n > 0$

$$x_{n+1} = -y_n \sqrt{a} \sin(\sqrt{a} \Delta) + x_n \cos(\sqrt{a} \Delta)$$

$$y_{n+1} = y_n \cos(\sqrt{a} \Delta) + \frac{x_n}{\sqrt{a}} \sin(\sqrt{a} \Delta)$$

where $a = a_6$ for $x > 0$ and $a = a'_6$ for $x < 0$.

REFERENCES

- [1] A. H. Boozer, "Physics of magnetically confined plasmas," *Rev. Mod. Phys.*, vol. 76, p. 1071, Jan. 2005.
- [2] S. Y. Medvedev *et al.*, "The negative triangularity tokamak: Stability limits and prospects as a fusion energy system," *Nucl. Fusion*, vol. 55, p. 063013, May 2015.
- [3] J. G. Cordey, R. J. Goldston, and R. R. Parker, "Progress toward a tokamak fusion reactor," *Phys. Today*, vol. 45, pp. 1–22, Jan. 1992.
- [4] I. Joseph *et al.*, "Calculation of stochastic thermal transport due to resonant magnetic perturbations in DIII-D," *Nucl. Fusion*, vol. 48, p. 045009, Mar. 2008.
- [5] T. Eich, A. Herrmann, and J. Neuhauser, "Nonaxisymmetric energy deposition pattern on ASDEX upgrade divertor target plates during type-I edge-localized modes," *Phys. Rev. Lett.*, vol. 91, p. 195003, Nov. 2003.
- [6] *Final Report of the ITER Engineering Design Activities*, ITER EDA document 21, IAEA, Vienna, Austria, Aug. 2001.
- [7] T. A. Casper, W. H. Meyer, L. D. Pearlstein, and A. Portone, "ITER shape controller and transport simulations," *Fusion Eng. Design*, vol. 83, pp. 552–556, Apr. 2008.
- [8] M. Brix *et al.*, "Accuracy of EFIT equilibrium reconstruction with internal diagnostic information at JET," *Rev. Sci. Instrum.*, vol. 78, p. 10F325, May 2008.
- [9] E. C. da Silva, I. L. Caldas, and R. L. Viana, "Field line diffusion and loss in a tokamak with an ergodic magnetic limiter," *Phys. Plasmas*, vol. 6, pp. 2855–2865, Mar. 2001.
- [10] E. C. da Silva, I. L. Caldas, and R. L. Viana, "The structure of chaotic magnetic field lines in a tokamak with external nonsymmetric magnetic perturbations," *IEEE Trans. Plasma Sci.*, vol. 29, no. 4, pp. 617–631, Aug. 2001.
- [11] S. S. Abdullaev *et al.*, "Overview of magnetic structure induced by the TEXTOR-DED and the related transport," *Nucl. Fusion*, vol. 43, no. 5, p. 299, Apr. 2003.
- [12] S. S. Abdullaev, K. H. Finken, M. Jakubowski, and M. S. Lehnen, "Mappings of stochastic field lines in poloidal divertor tokamaks," *Nucl. Fusion*, vol. 46, no. 4, p. S113, Mar. 2006.
- [13] S. S. Abdullaev, "Model of a magnetic field in poloidal divertor tokamaks affected by resonant magnetic perturbations," *Phys. Plasmas*, vol. 16, p. 030701, Oct. 2009.
- [14] S. S. Abdullaev, "Stable and unstable manifolds, and the structure of magnetic footprints," *Nucl. Fusion*, vol. 54, pp. 064004-1–064004-11, May 2014.
- [15] S. S. Abdullaev, "Canonical maps near separatrix in Hamiltonian systems," *Phys. Rev. E, Stat. Phys. Plasmas Fluids Relat. Interdiscip. Top.*, vol. 70, p. 046202, Oct. 2004.
- [16] A. Punjabi, A. Verma, and A. Boozer, "Stochastic broadening of the separatrix of a tokamak divertor," *Phys. Rev. Lett.*, vol. 69, p. 3322, Dec. 1992.
- [17] A. Punjabi, H. Ali, and A. Boozer, "Symmetric simple map for a single-null divertor tokamak," *Phys. Plasmas*, vol. 4, pp. 337–346, Jan. 1997.
- [18] A. Punjabi, H. Ali, and A. Boozer, "Effects of dipole perturbation on the stochastic layer and magnetic footprint in single-null divertor tokamaks," *Phys. Plasmas*, vol. 10, pp. 3992–4003, Sep. 2003.
- [19] H. Ali, A. Punjabi, A. Boozer, and T. Evans, "The low MN map for single-null divertor tokamaks," *Phys. Plasmas*, vol. 11, pp. 1908–1919, Apr. 2004.
- [20] A. Punjabi, H. Ali, T. Evans, and A. Boozer, "Modeling of stochastic broadening in a poloidally diverted discharge with piecewise analytic symplectic mapping flux functions," *Phys. Plasmas*, vol. 15, p. 082507, Aug. 2008.
- [21] A. Punjabi and A. Ali, "Symplectic approach to calculation of magnetic field line trajectories in physical space with realistic magnetic geometry in divertor tokamaks," *Phys. Plasmas*, vol. 15, p. 122502, Dec. 2008.
- [22] A. Punjabi and A. Ali, "An accurate symplectic calculation of the inboard magnetic footprint from statistical topological noise and field errors in the DIII-D," *Phys. Plasmas*, vol. 18, p. 022509, Feb. 2011.
- [23] A. Punjabi and A. Boozer, "Homoclinic tangle in tokamak divertors," *Phys. Lett. A*, vol. 278, pp. 2410–2416, Jun. 2014.
- [24] A. Punjabi, "Homoclinic tangle of the ideal separatrix in the DIII-D tokamak from (30, 10) + (40, 10) perturbation," *Phys. Plasmas*, vol. 21, pp. 122516-1–122516-13, Dec. 2014.
- [25] T. Kroetz, M. Roberto, I. L. Caldas, R. L. Viana, P. J. Morrison, and P. Abbamonte, "Integrable maps with non-trivial topology: Application to divertor configurations," *Nucl. Fusion*, vol. 50, p. 034003, Feb. 2010.
- [26] T. Kroetz, M. Roberto, I. L. Caldas, R. L. Viana, and P. J. Morrison, "Divertor map with freedom of geometry and safety factor profile," *Plasma Phys. Control. Fusion*, vol. 54, p. 045007, Mar. 2012.
- [27] F. Karger and K. Lackner, "Resonant helical divertor," *Phys. Lett. A*, vol. 61, pp. 385–387, Jun. 1977.
- [28] W. Engelhardt and W. Feneberg, "Influence of an ergodic magnetic limiter on the impurity content in a tokamak," *J. Nucl. Mater.*, vols. 76–77, pp. 518–520, Oct. 1978.
- [29] W. Feneberg and G. H. Wolf, "A helical magnetic limiter for boundary layer control in large tokamaks," *Nucl. Fusion*, vol. 21, no. 6, p. 669, 1981.
- [30] A. Vannucci, I. C. Nascimento, and I. L. Caldas, "Disruptive instabilities in the discharges of the TBR-1 small tokamak," *Plasma Phys. Controlled Fusion*, vol. 31, no. 2, p. 147, 1989.
- [31] C. J. A. Pires, E. A. O. Saettone, M. Y. Kucinski, A. Vannucci, and R. L. Viana, "Magnetic field structure in the TCABR tokamak due to ergodic limiters with a non-uniform current distribution: Theoretical and experimental results," *Plasma Phys. Control Fusion*, vol. 47, p. 1609, Sep. 2005.
- [32] T. J. Martin and J. B. Taylor, "Ergodic behaviour in a magnetic limiter," *Plasma Phys. Control. Fusion*, vol. 26, p. 321, Oct. 1984.
- [33] R. K. W. Roeder, B. I. Rapoport, and T. E. Evans, "Explicit calculations of homoclinic tangles in tokamaks," *Phys. Plasmas*, vol. 1, p. 3796, Aug. 2003.
- [34] A. Wingen, T. E. Evans, and K. H. Spatschek, "High resolution numerical studies of separatrix splitting due to non-axisymmetric perturbation in DIII," *Nucl. Fusion*, vol. 49, p. 042504, Apr. 2009.
- [35] T. E. Evans, R. K. W. Roeder, J. A. Carter, B. I. Rapoport, M. E. Fenstermacher, and C. J. Lasnier, "Experimental signatures of homoclinic tangles in poloidally diverted tokamaks," *J. Phys. Conf. Ser.*, vol. 7, no. 7, p. 174, Apr. 2005.
- [36] H. Frerichs, O. Schmitz, D. Reiter, T. E. Evans, and Y. Feng, "Striation pattern of target particle and heat fluxes in three dimensional simulations for DIII-D," *Phys. Plasmas*, vol. 21, p. 020702, Feb. 2014.
- [37] A. Kirk, J. Harrison, Y. Liu, E. Nardon, I. T. Chapman, P. Denner, and The MAST Team, "Observation of lobes near the X point in resonant magnetic perturbation experiments on MAST," *Phys. Rev. Lett.*, vol. 108, p. 255003, Jun. 2012.
- [38] P. Beaufume, M. A. Dubois, and M. S. M. Benkadda, "Diffusion in the noisy Chirikov–Taylor mapping," *Phys. Lett. A*, vol. 147, pp. 87–91, Jul. 1990.
- [39] A. B. Schelin, I. L. Caldas, R. L. Viana, and S. Benkadda, "Collisional effects in the tokamak," *Phys. Lett. A*, vol. 376, pp. 24–30, Nov. 2011.
- [40] J. F. Artaud *et al.*, "The CRONOS suite of codes for integrated tokamak modelling," *Nucl. Fusion*, vol. 50, p. 043001, Mar. 2010.
- [41] T. Kroetz, C. G. L. Martins, M. Roberto, and I. L. Caldas, "Set of wires to simulate tokamaks with poloidal divertor," *J. Plasma Phys.*, vol. 79, pp. 751–757, Apr. 2013.

Geraldo Roberson received the B.Sc. degree in physics from the Federal University of Pernambuco, Recife, Brazil, and the M.Sc. degree in plasma physics from the Technological Institute of Aeronautics, São Jose dos Campos, Brazil, where he is currently pursuing the Ph.D. degree in sciences and space technologies.

Marisa Roberto received the B.S. degree in physics from the Catholic University of São Paulo, São Paulo, Brazil, in 1982, the M.S. degree from the Space Research Institute, São Jose dos Campos, Brazil, in 1986, and the Ph.D. degree in plasma physics from the Aeronautic Institute of Technology (ITA), in São Jose dos Campos, in 1992.

In 1999 and 2004, she was a Visiting Scholar with the University of California at Berkeley, Berkeley, CA, USA. She is currently a Full Professor with the Physics Department, ITA. Her current research interests include plasma physics for technological applications and chaos.

Iberê Luiz Caldas was born in Santos, Brazil, in 1948. He received the B.S. and Ph.D. degrees in physics from the Institute of Physics of University of São Paulo (IF-USP), São Paulo, Brazil, in 1970 and 1979, respectively.

In 1977, 1979, 1983, 1984, and 1988, he was a Guest Scientist with the Max-Planck-Institut fuer PlasmaPhysik, Garching bei München, Germany. Since 1995, he has been a Full Professor with IF-USP. His current research interests include plasma physics and chaos.

Ricardo Luiz Viana received the Ph.D. degree in plasma physics from the Institute of Physics, Universidade de São Paulo, Brazil, in 1991.

In 1987, he was a Visiting Scholar with the Institute for Physical Science and Technology, University of Maryland, College Park, MD, USA. He has been a Professor with the Physics Department, Universidade Federal do Paraná Curitiba, Curitiba, Brazil, since 1989. He has authored 190 papers and supervised ten doctoral theses, and three post-doctoral works.

Tiago Kroetz received the Ph.D. degree in plasma physics from the Instituto Tecnológico de Aeronáutica, São José dos Campos, Brazil, in 2010.

Since 2010, he has been involved in research about nonlinear dynamics applied to plasma physics and mechanical systems, and also extended to the field of research on the physics education. He has been a Professor with the Physics Academic Department, Universidade Tecnológica Federal do Paraná, Pato Branco, Brazil, since 2012.